Photodissociation and photoisomerization pathways of the HNCN free radical

Ryan T. Bise,[a] Alexandra A. Hoops, and Daniel M. Neumark[b]
Department of Chemistry, University of California, Berkeley, California 94720
and Chemical Sciences Division, Lawrence Berkeley National Laboratory, Berkeley, California 94720

(Received 22 January 2001; accepted 5 March 2001)

The photodissociation spectroscopy and dynamics of the HNCN free radical have been investigated by fast beam photofragment translational spectroscopy. Predissociative transitions for both the $\tilde{B}\ ^2A' \leftarrow \tilde{X}\ ^2A''$ band and a higher-energy band system assigned to the $\tilde{C}\ ^2A'' \leftarrow \tilde{X}\ ^2A''$ band were observed. Photofragment mass distributions indicate that N_2 loss is the primary dissociation pathway. Translational energy distributions reveal a resolved vibrational structure of the N_2 fragment, suggesting that the HNCN radical first isomerizes to a cyclic HCN_2 intermediate. A dissociation mechanism is proposed in which electronically excited HNCN undergoes internal conversion to the ground state, followed by isomerization to cyclic HCN_2 and dissociation through a tight three-center transition state. The HNCN bond dissociation energy D_0 and heat of formation $\Delta_f H_0$(HNCN) were determined to be 2.80 ± 0.03 eV and 3.35 ± 0.03 eV, respectively. © *2001 American Institute of Physics.* [DOI: 10.1063/1.1367411]

I. INTRODUCTION

In this paper we present a study of the photodissociation dynamics and spectroscopy of the HNCN radical. This radical and other HCN_2 structural isomers have been proposed as intermediates in the $CH+N_2$ reaction, an important reaction in hydrocarbon combustion because of its possible role in the formation of ''prompt'' NO.[1–5] Specifically, this reaction may provide a low-energy pathway for the splitting of molecular nitrogen via $CH(^2\Pi) + N_2 \rightarrow HCN + N(^4S)$, the initiating step of the Fenimore mechanism[1,6,7] for prompt NO formation; the N and HCN products are subsequently oxidized rapidly by O atoms and OH radicals to form nitric oxide. Although the initial reaction is only endothermic by less than 0.1 eV, it is spin forbidden.

The $CH+N_2$ reaction has been studied in detail both experimentally[1,3,5,8] and theoretically.[2,3,9–18] Early experimental work on this reaction has been reviewed by miller and Bowman.[2] More recent shock tube studies by Dean *et al.*[5] and Lindackers *et al.*[8] have directly detected the $N(^4S)$ atom and show that the $N(^4S)$ atom appearance is correlated with the removal of CH. Numerous theoretical studies[9–12,15] indicate that the reaction pathway with the highest probability proceeds through an intermediate doublet cyclic HCN_2(c-HCN_2) adduct. This then undergoes intersystem crossing to a quartet surface and finally dissociates to quartet products $N(^4S) + HCN$. However, recent calculations by Cui *et al.*[12] find the thermal rate constant $k(T)$ to be two orders of magnitude lower than experimental results due to the slow ISC rate. This result led to a new mechanism proposed by Lin and co-workers[13,19] for N and NO production, in which the c-HCN_2 adduct isomerizes to the lower-energy HNCN isomer. This dissociates to spin-allowed $H(^2S) + NCN(\tilde{X}\ ^3\Sigma_g^-)$ products, with N and NO formed by subsequent reactions of the NCN product.

In an effort to further characterize the global $CH+N_2$ potential energy surface and assess the importance of the HNCN radical as a possible intermediate in the $CH+N_2$ reaction, we have investigated the photodissociation spectroscopy and dynamics of the HNCN radical. The work presented here represents part of an ongoing study of radicals (NCN, CNN, HCNN)[20–22] that may play a role in the reactions of N_2 in flames leading to NO production.

HNCN is the most stable HCN_2 isomer. Previous studies by Clifford *et al.*[23] indicate that the structural isomer HNCN lies more than 2.8 eV below $CH+N_2$ products, compared to 1.13 eV for lin-HCNN[21] and 1.02 eV for c-HCN_2.[11,12] The HNCN radical was first identified spectroscopically by Herzberg and Warsop,[24] who reported a rotationally resolved $^2A' \leftarrow {}^2A''$ electronic absorption ($T_0 = 28\,994\ cm^{-1}$). They determined the molecular structure for both the ground and excited states and assigned this absorption to the $\tilde{B}\ ^2A' \leftarrow \tilde{X}\ ^2A''$ band of HNCN. The HNC bond angle for the ground state was found to be 116.5° with a nearly linear NCN backbond. Wu *et al.*[25] probed the $\tilde{B}\ ^2A' \leftarrow \tilde{X}\ ^2A''$ origin with laser-induced fluorescence, determining the excited state lifetime to be 20 ± 5 ns. Dispersed fluorescence showed the symmetric stretch ($\nu_2 = 1140\ cm^{-1}$) and the δ(HN–C–N) a'' mode ($\nu_6 \approx 440\ cm^{-1}$) to be vibronically active; the ν_6 mode was attributed to vibronic coupling via a Renner–Teller-type interaction. Travis and Herzberg[26] reported higher-energy absorption bands at 30 475 and 31 550 cm^{-1} from the flash photolysis of diazomethane, showing complicated subband structure that shifts upon deuteration. These higher-energy absorption bands have been observed using a variety of photolysis sources by Basco and Yee,[27]

[a]Current address: Bell Laboratories, Lucent Technologies, 600–700 Mountain Avenue, Murray Hill, New Jersey 07974.
[b]Author to whom correspondence should be addressed. Electronic mail: dan@radon.cchem.berkeley.edu

 © 2001 American Institute of Physics

Downloaded 01 Jun 2001 to 128.32.220.22. Redistribution subject to AIP license or copyright, see http://ojps.aip.org/jcpo/jcpcr.jsp

Kroto and co-workers,[28] and Mathews *et al.*[29]

The microwave spectrum of HNCN measured by Yamamoto and Saito[30] showed that the unpaired electron occupies an orbital perpendicular to the molecular plane of symmetry and yielded an estimated energy difference of approximately 1.5 eV between the Renner–Teller $\tilde{X}\ ^2A''$ and $\tilde{A}\ ^2A'$ pair. Photoelectron studies by Clifford *et al.*[23] of the $HNCN^{-1}$ anion yielded the electron affinity of HNCN (EA=2.622 ±0.005 eV) and vibrational frequencies of 1049±162 and 1879±106 cm^{-1} for the ν_2 and ν_3 modes, respectively, in reasonable agreement with matrix infrared[31] and the dispersed fluorescence studies.[25] Higher-energy photoelectron studies performed in our laboratory[32] have located the $\tilde{A}\ ^2A'$ state, finding the $\tilde{X}\ ^2A''-\tilde{A}\ ^2A'$ splitting to be 0.7 eV. Unlike the $\tilde{X}\ ^2A''$ state, which displays a nearly vertical photodetachment spectrum showing little vibrational excitation, the $\tilde{A}\ ^2A'$ state yields a broad band (~1 eV in width). No regular vibrational structure was observed for this state.

Ab initio calculations of the molecular geometry and vibrational frequencies of the HNCN ground state were first performed by Tao *et al.*[33] and, more recently, by several other groups.[11,12,19,23] The calculations are in reasonable agreement with the experimental vibrational frequencies given above. The calculations support an acetylenic structure showing a shorter HNC≡N bond and longer HN–CN bond with HNC bond angles between 110.8° to 113.6° and a nearly linear NCN bond angle of 175°, in good agreement with the spectroscopic results of Herzberg and Travis.[24]

The HNCN radical provides an intriguing system for photodissociation studies, with several relatively low-lying product channels. Based on this work and accepted literature values, the heats of reaction (at 0 K), $\Delta_{rsn}H_0$, for the five lowest-energy product channels are as follows:

$$\mathrm{HNCN}(\tilde{X}\ ^2A'') \xrightarrow{h\nu}$$

$$\mathrm{N_2}(\tilde{X}\ ^1\Sigma_g^+)+\mathrm{CH}(\tilde{X}\ ^2\Pi) \quad 2.80\pm0.03\ \mathrm{eV} \quad \text{(I)}$$

$$\mathrm{HCN}(\tilde{X}\ ^1\Sigma^+)+\mathrm{N}(^4S) \quad 2.87\pm0.05\ \mathrm{eV} \quad \text{(II)}$$

$$\mathrm{HNC}(\tilde{X}\ ^1\Sigma^+)+\mathrm{N}(^4S) \quad 3.45\pm0.05\ \mathrm{eV} \quad \text{(III)}$$

$$\mathrm{N_2}(\tilde{X}\ ^1\Sigma_g^+)+\mathrm{CH}(\tilde{a}\ ^4\Sigma) \quad 3.54\pm0.03\ \mathrm{eV} \quad \text{(IV)}$$

$$\mathrm{H}(^2S)+\mathrm{NCN}(\tilde{X}\ ^3\Sigma_g^-) \quad 3.72\pm0.04\ \mathrm{eV} \quad \text{(V)}.$$

Dissociation to the lowest-energy channels [(I)–(IV)] requires substantial bond rearrangement and/or intersystem crossing (ISC) to quartet surfaces.

The photofragmentation studies performed here show that vibronic levels of both the $\tilde{B}\ ^2A'$ state and the higher-energy band system (31 200–34 700 cm^{-1}) assigned to the $\tilde{C}\ ^2A''$ state are predissociative. Photofragment mass distributions show $CH+N_2$ to be the primary dissociation channel. Translational energy distributions display a resolved structure corresponding to vibrational excitation of the N_2 photofragment. The formation of N_2 in the photolysis of HNCN suggests that this radical is a likely intermediate in the $CH+N_2$ reaction.

II. EXPERIMENT

The fast beam photofragment translational spectrometer[34–36] used in these studies is shown in Fig. 1. Vibrationally and rotationally cold neutral radicals are produced by mass-selectively photodetaching a beam of stable negative ions. The neutral radicals are then photodissociated by a second laser and the photofragments are detected directly with high efficiency.

The ion source configuration for $HNCN^-$ was the same as that previously used for NCN^-.[37,38] Argon at a stagnation pressure of ~2 atm is expanded through a pulsed molecular beam valve into a reservoir containing cyanamide at room temperature and then through a pulsed electric discharge, generating mainly CN^-, NCN^-, and $HNCN^-$ ions. Previous studies[20] indicate that this source typically produces anions with rotational and vibrational temperatures of 50 and 200 K, respectively. D_2NCN was synthesized by repeated washing of the cyanamide crystals with a methanol-d_4/acetic acid-d_4 solution (20:1 by volume) followed by evaporation of the solvent. From our ion mass distributions, we estimate the extent of deuteration to be ⩽40%.

The negative ions generated in the source region are accelerated to 8 keV and separated temporally by a Bakker time-of-flight (TOF) mass spectrometer[39,40] with a mass resolution $(m/\Delta m)\approx 100$. The ion of interest is selectively photodetached by a pulsed dye laser. To generate vibrationally cold radicals, an excimer pumped dye laser is tuned to 2.74 eV, which is 118 meV above the detachment threshold based upon the photoelectron spectrum of Clifford *et al.*[23] Undetached ions are deflected out of the beam path.

In the dissociation region, the fast beam of neutrals are intersected by a second excimer-pumped dye laser. A fraction of the neutrals absorb and dissociate yielding photofragments detected directly by either the TOF or TPS (time and position sensing) microchannel plate detector assemblies shown in Fig. 1. An aluminum strip is positioned at the center of each detector to prohibit undissociated radicals from impacting the detector, so that the observed signal is entirely from recoiling photofragments.

Two types of experiments are performed. First, the spectroscopy of the dissociative electronic states is examined by scanning the dissociation laser and monitoring the total flux of photofragments arriving at the retractable TOF detector, located 0.68 m from the dissociation laser. The resulting photofragment yield (PFY) spectra is complementary to absorption and fluorescence measurements. We examined the photolysis of the HNCN radical from 28 800 to 34 850 cm^{-1}.

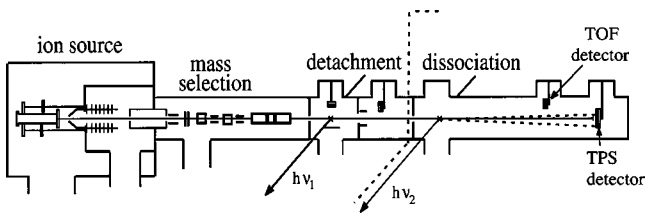

FIG. 1. Fast beam photofragment translational spectrometer. The dotted line separates the radical production section on the left from the photodissociation experiment on the right.

Downloaded 01 Jun 2001 to 128.32.220.22. Redistribution subject to AIP license or copyright, see http://ojps.aip.org/jcpo/jcpcr.jsp

The fundamental output of the dye laser with a bandwidth of 0.2 cm^{-1} was used to cover the $\tilde{B}\ ^2A' \leftarrow \tilde{X}\ ^2A''$ band from 28 800 to 29 850 cm^{-1} while the dye laser output was frequency doubled using KDP-R6G and BBO-B crystals to cover frequencies from 29 850 to 34 850 cm^{-1} with a laser bandwidth of 0.3 cm^{-1}. Saturation and power-broadening effects were observed for the $\tilde{B}\ ^2A' \leftarrow \tilde{X}\ ^2A''$ band at laser fluences >30 mJ/cm^2, and it was therefore scanned at fluences <20 mJ/cm^2. No noticeable saturation effects were seen for the higher-energy transitions.

Once the spectroscopy of the dissociative states has been examined, the dissociation dynamics at selected photolysis energies are investigated. In this experiment, both photofragments from a single parent radical are detected in coincidence using a TPS detector based upon the concept developed by de Bruijn and Los.[41] This detection scheme has been described in detail elsewhere.[34,35] The TPS detector records the positions and difference in arrival time of the two photofragments from a single dissociation event. This information is then used to determine the masses of the fragments, their relative translational energy, E_T, and the scattering angle θ between the relative velocity vector of the polarized dissociation laser. This coincident detection scheme requires that photofragment mass ratio be less than 4. The photofragment mass resolution, $m/\Delta m$, is ≈ 10 and the translational energy resolution is $\Delta E_T/E_T = 2.0\%$. As discussed in a previous paper,[20] the relatively poor mass resolution for the photofragments is due to the ~ 1 mm diameter of the radical beam at the TPS detector.

III. RESULTS

A. Photofragment yield spectra

1. $\tilde{B}\ ^2A' \leftarrow \tilde{X}\ ^2A''$ transitions

Photofragment yield spectra for the $\tilde{B}\ ^2A' \leftarrow \tilde{X}\ ^2A''$ band are displayed in Figs. 2(a) and 2(b). Figure 2(a) shows the photofragment yield spectra between 28 850 to 29 170 cm^{-1} and displays sharp, intense features separated by ~ 40 cm^{-1}, consistent with the $\tilde{B}\ ^2A' \leftarrow \tilde{X}\ ^2A''$ origin transition first observed in higher resolution absorption and LIF experiment by Herzberg and Warsop[24] and Wu *et al.*,[25] respectively. The band displays features characteristic of a perpendicular transition for a nearly prolate symmetric top: a series of subbands each with a sharp Q branch and weaker P and R branches. Each Q branch is labeled $K_a' - K_a''$, indicating the excited and ground state quantum numbers K_a' and K_a'', respectively; the spectrum is dominated by $\Delta K_a = \pm 1$ transitions, as expected for a nearly prolate top. A fit to the rotational contour for the P and R branches of the 2-1 subband yields a temperature of ~ 60 K for rotation about the *b* and *c* axes. The intensity distribution of the Q branches reveals a hotter distribution with a characteristic temperature of ~ 200 K. Note that the 2-1 Q branch is about twice as intense as the 0-1 Q branch because twice as many transitions contribute to it.[42]

Figure 2(b) shows a new weak band located ~ 560 cm^{-1} to the blue of the origin band. The most intense features are spaced by approximately 80 cm^{-1}, twice that observed for the origin band, and display broader rotational contours than the origin band. The band is attributed to a parallel vibronic transition (see Sec. IV A) with K_a selection rules $\Delta K_a = 0, \pm 2, 4, \ldots$. The subband K_a values are labeled using the same notation described above for the $\tilde{B}\ ^2A' \leftarrow \tilde{X}\ ^2A''$ origin transition.

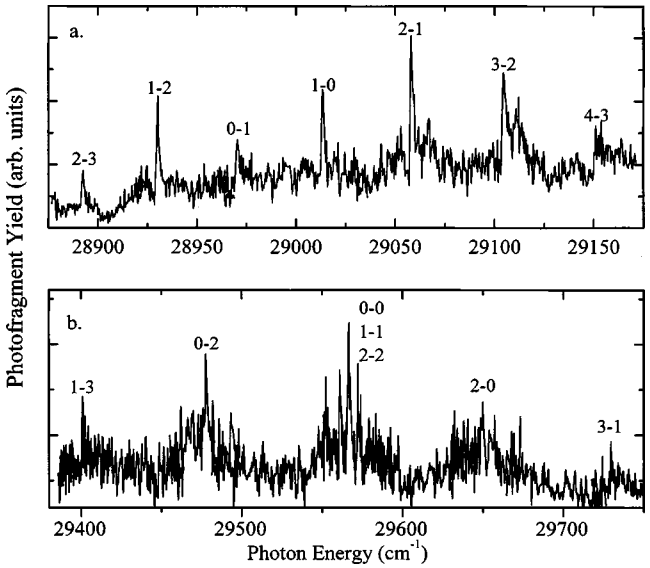

FIG. 2. (a) Photofragment yield (PFY) spectrum of the HNCN $\tilde{B}\ ^2A' \leftarrow \tilde{X}\ ^2A''$ vibronic origin, showing $\Delta K_a = \pm 1$ transitions. K_a stacks are labeled $K_a' - K_a''$. (b) PFY spectra of the higher-energy vibronic band of the $\tilde{B}\ ^2A' \leftarrow \tilde{X}\ ^2A''$ transition. This band is assigned to excitation of the δ(HN–C–N) a'' ν_6 bend mode.

2. Higher-energy transitions

Higher-energy transition originate near 31 500 cm^{-1} and form a progression spaced by about 1000 cm^{-1}, as shown in Fig. 3(a), with the most intense feature located near 32 500 cm^{-1}. A detailed list of the transition energies and relative intensities for the HNCN and DNCN photofragment yield spectra is given in Table I, with the vibrational spacing defined as the energy difference between the intensity maxima of each vibronic transition. The observed PFY transitions are consistent with a number of previously reported absorption bands.[26–29] Despite extensive scanning, we were unable to observe the lowest previously reported member of this progression near 30 475 cm^{-1}.[26,29]

Expanded views of the transitions at 31 550 and 32 550 cm^{-1} are shown in Fig. 3(b). As can be seen in Figs. 3(a) and 3(b), the subband structure of the 31 500 cm^{-1} transition is remarkably different from the higher-energy transitions; it is comprised of three main subbands of nearly equal intensity spaced by ~ 24 cm^{-1} that are denoted *X*, *Y*, and *Z* following the labeling scheme of Mathews *et al.*[29] Feature *X* is split into three main peaks split by nearly 5 and 7 cm^{-1}, while *Y* shows smaller splittings of 2 and 3 cm^{-1}. Feature *Z* is split into a doublet with a peak separation of 6 cm^{-1}. The observed subband structure for this transition is in excellent agreement with that observed by Kroto and co-workers[28] and by Mathews *et al.*[29]

Downloaded 01 Jun 2001 to 128.32.220.22. Redistribution subject to AIP license or copyright, see http://ojps.aip.org/jcpo/jcpcr.jsp

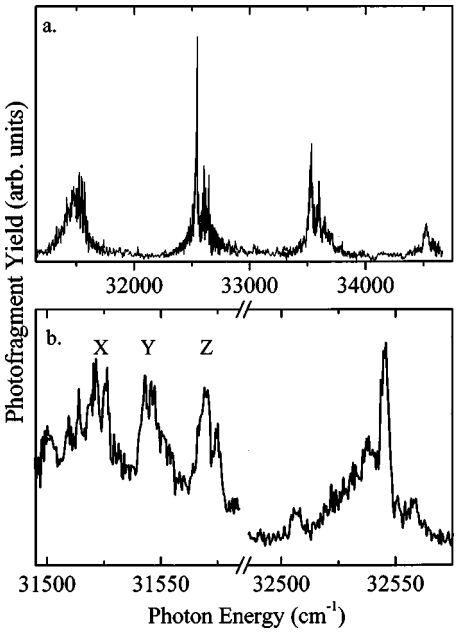

FIG. 3. (a) PFY spectra of the HNCN radical from 31 000–35 000 cm^{-1}. This band has been assigned to the $\tilde{C}\ ^2A''\leftarrow\tilde{X}\ ^2A''$ band. (b) Expanded views of the 31 550 and 32 550 cm^{-1} vibronic transitions. For the 31 550 cm^{-1} band three major subbands are labeled *X*, *Y*, and *Z* and are spaced by $\sim$24 cm^{-1}.

Higher-energy members of this progression, of which the 32 550 cm^{-1} band in Fig. 3(b) is an example, are dominated by an intense peak to the red that is strongly red-degraded. Less intense subbands [not shown in Fig. 3(b)] are located to the blue and do not display any regular subband spacing. The FWHM of the most intense subbands of each vibronic transition increases with photon energy, with values of 5, 10, and 50 cm^{-1}, respectively, for the features at 32 545, 33 524, and 34 525 cm^{-1}.

TABLE I. Photofragment yield transition energies for HNCN and DNCN.

HNCN			DNCN		
Transition (cm^{-1})	Relative intensity	Vibrational spacing (cm^{-1})	Transition (cm^{-1})	Relative intensity	Vibrational spacing (cm^{-1})
31 521	5		31 506	10	
31 526	5		31 522	8	
31 543	5		31 531	6	
31 545	5				
31 547	5				1036
31 568	5		32 542	8	
31 574	4				
		1024			
31 505	2				
32 538	6				
32 545	10				
32 603	4				
32 620	3				
32 640	3				
32 645	3				
		989			
33 521	4				
33 534	5				
33 601	3				
33 644	2				
		991			
34 525	1.3				

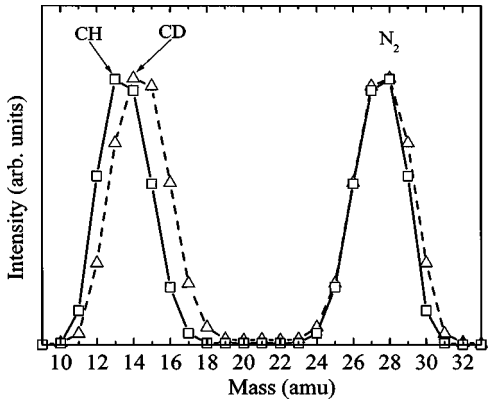

FIG. 4. Photofragment mass distributions for the fragmentation of HNCN (squares) and DNCN (triangles) at 3.9 eV showing the photoproducts to be $CH(CD)+N_2$.

For DNCN (not shown), transitions were observed near 31 530 and 32 547 cm^{-1} that are strongly red degraded. The peak positions are similar to those observed for HNCN showing no real isotope effect. A significant isotope effect is observed for the subband structure of the 31 530 cm^{-1} band with peak spacings of 9 and 16 cm^{-1} compared to 24 cm^{-1} for HNCN, indicating that this subband structure is due to the rotational K_a structure. Only a single red degraded peak is seen for the 32 547 cm^{-1} transitions. These observations are again in excellent agreement with the absorption studies of Kroto and co-workers[28] and Mathews *et al.*[29]

B. Photofragment mass distributions

Figure 4 shows the photofragment mass distributions for HNCN and DNCN for a photon energy of 3.9 eV. Our photofragment mass resolution is only $m/\Delta m\approx 10$, so from the HNCN distribution alone it is difficult to distinguish between $CH+N_2$ products (13:28 mass ratio) and N+HCN products (14:27). Note that these channels are quite close energetically (see the Introduction) so one does not expect to be able to use the product kinetic energy distributions to identify the mass channel. However, an unambiguous determination results from a comparison with DNCN photodissociation, for which both product channels yield a mass ratio of 14:28. The width of the mass distributions for HNCN is identical to that for DNCN, indicating that only one mass channel contributes. In addition, the mass of the light photofragment from HNCN is one mass unit lower than that from DNCN, whereas the heavy fragment mass is the same. Hence $CH+N_2$ must be the dominant product channel in Fig. 4. Although the H-loss channel is energetically available for transitions greater than 3.72 eV, our coincident detection scheme requires a photofragment mass ratio <4 and we are therefore insensitive to the H-loss channel.

C. Photofragment translational energy distributions

The translational energy $P(E_T)$ distributions for the $\tilde{B}\ ^2A'\leftarrow\tilde{X}\ ^2A''$ origin band and the higher-energy transitions

Downloaded 01 Jun 2001 to 128.32.220.22. Redistribution subject to AIP license or copyright, see http://ojps.aip.org/jcpo/jcpcr.jsp

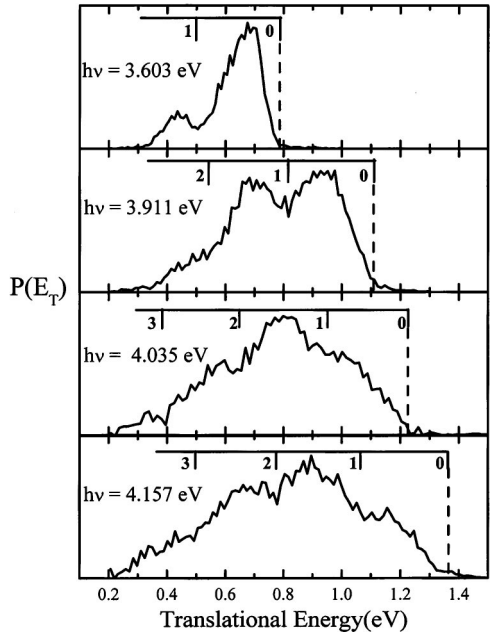

FIG. 5. Translational energy $P(E_T)$ distributions for $CH+N_2$ photofragments. Photon energies are given and maximum translational energies E_T^{max} are indicated with dashed vertical lines. Energetic onsets for the vibrational states of the N_2 fragment are denoted with a comb.

are shown for HNCN and DNCN in Figs. 5 and 6. Distributions for HNCN and DNCN at the same photon energies are quite similar. All the distributions display sharp onsets at high translational energy and reveal structured features with peak separations ranging from 220 to 260 meV. For HNCN, the $P(E_T)$ distribution from excitation at 3.603 eV displays a particularly sharp onset at 0.795 eV. A similarly sharp onset at 0.763 eV is seen in the $P(E_T)$ distribution for DNCN photodissociation at 3.599 eV. We assume these onsets define the maximum translational energy, E_T^{max}, corresponding to fragments with zero internal energy. The corresponding values of E_T^{max} at higher photon energies for HNCN and DNCN, shown by dashed vertical lines in Figs. 5 and 6, agree very well with the onset of signal in the $P(E_T)$ distributions, strongly supporting our assumption of thermodynamic significance to E_T^{max}. A very weak signal observed above E_T^{max} in some of the distributions is attributed to photoexcitation from vibrationally excited levels of the ground electronic state.

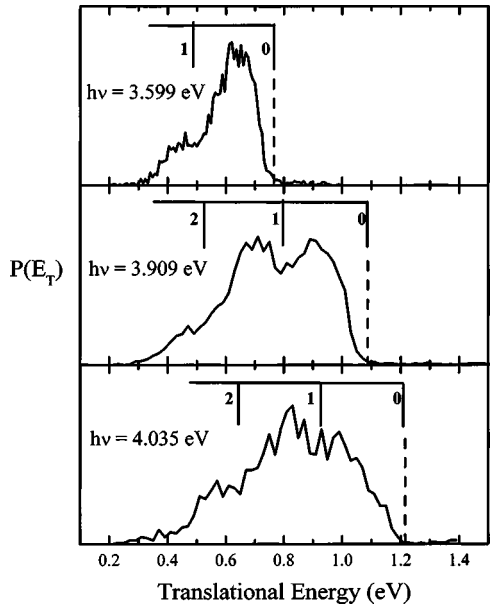

FIG. 6. $P(E_T)$ distributions for the $CD+N_2$ from DNCN photodissociation. Photon energies are given and maximum translational energies E_T^{max} are indicated with dashed vertical lines. Energetic onsets for the vibrational states of the N_2 fragment are denoted with a comb.

The structure of the $P(E_T)$ distributions reflect the internal energy distribution of the nascent $N_2+CH(CD)$ photofragments. The observed structure with an energy separation of ~250 meV can be reasonably assigned to the vibrational excitation of the N_2 photofragment. A further comment on the internal energy distribution of the photofragments will be made in Sec. IV B.

The distributions change noticeably with increased photon energy. For HNCN, the lowest-energy transition displays two major features peaked at 0.67 and 0.44 eV, respectively, with the former comprising ~85% of the total distribution, with FWHM=150 meV and a slight symmetry to lower translational energy. The width of the corresponding feature for DNCN, peaked at 0.73 eV, is slightly broader, FWHM =170 meV. At higher excitation energies the overall widths of the $P(E_T)$ distributions increase and the structured features are considerably broader. The higher-energy distributions are not as sharply peaked toward high translational energy, e.g., excitation at 4.035 and 4.157 eV for HNCN yields $P(E_T)$ distributions peaked 0.44 and 0.46 eV below the maximum translational energy. For all photon energies, the angular distributions were found to be nearly isotropic.

IV. ANALYSIS

A. Photofragment yield spectra

1. $\tilde{B}\,^2A' \leftarrow \tilde{X}\,^2A''$ transitions

The $\tilde{B}\,^2A' \leftarrow \tilde{X}\,^2A''$ origin, observed in this work via photofragment yield spectroscopy, Fig. 2(a), has been characterized previously in higher resolution absorption[24] and emission studies.[25] In this section, we will therefore focus our attention toward the new band observed in our PFY spectra centered ~560 cm^{-1} to the blue of the origin [Fig. 2(b)]. Wu *et al.*[25] determined the *a*-axis rotational constants for the $\tilde{X}\,^2A''$ and $\tilde{B}\,^2A'$ states to be 21.298 and 22.300 cm^{-1}, respectively. The rotational subband spacing in Fig. 2(a) is nearly 80 cm^{-1}, approximately $4A'$, consistent with $\Delta K_a = \pm 2$ transitions, suggesting a parallel-type transition with K_a selection rules $\Delta K_a = 0, \pm 2, 4, \ldots$. The subband spacing is larger toward the blue, in agreement with the upper state *a*-axis rotational constant being slightly larger than that for the ground state. Based upon the K_a subband spacing and intensity, we assign the largest feature near 29 570 cm^{-1} to overlapped $\Delta K_a = 0$ bands with contributions expected from $K_a = 0,1,2$, and 3 branches. The exact positions of the individual $\Delta K_a = 0$ bands cannot be clearly ascertained from our spectrum. The rotational contours of each subband are broad, lacking the sharp intense Q branch features observed

Downloaded 01 Jun 2001 to 128.32.220.22. Redistribution subject to AIP license or copyright, see http://ojps.aip.org/jcpo/jcpcr.jsp

for the origin band. The broader rotational contours are consistent with a parallel vibronic transition. While the $\Delta K_a = 0$ bandhead is most intense, the $\Delta K_a = \pm 2$ subbands show considerable intensity. The energy spacing of 560 cm^{-1} from the origin suggests that this band involves an HN–C–N bend mode and the parallel band structure indicates that the overall vibronic symmetry of this band is the same as the ground state, A''.

An analogous parallel band, centered at ~440 cm^{-1} to the red of the $\tilde{B}\ ^2A' \rightarrow \tilde{X}\ ^2A''$ has been observed in dispersed fluorescence measurements by Wu *et al.*[25] As in our spectra, the $\Delta K_a = \pm 2$ subbands show significant intensity. The authors assign this band to the out of plane bend mode, δ(HN–C–)a'', of the ground state and suggest that this band becomes active via a Renner–Teller-type mechanism in which the $\tilde{X}\ ^2A''$ and $\tilde{A}\ ^2A'$ bands are contaminated by the $\tilde{B}\ ^2A'$ state, giving the $\tilde{X}\ ^2A''$ states some A' character. These authors argue that the mechanism is similar to the Renner–Teller interaction described by Bolman and Brown[43] to account for the ''forbidden'' parallel bands in the analogous $\tilde{A}\ ^2\Sigma^+ - \tilde{X}\ ^2\Pi$ band system of NCO. We propose that a similar Renner–Teller interaction is responsible for the parallel vibronic band centered about 560 cm^{-1} to the blue of the $\tilde{B}$ state origin in which the zero-point vibrational level of the $\tilde{X}\ ^2A''$ state is mixed with vibrational states of the $\tilde{B}\ ^2A''$ state with a'' character. The parallel band is accordingly assigned to the out of plane bend, δ(HN–C–), an a'' mode of the $\tilde{B}\ ^2A'$ state with an estimated frequency of 560 ± 10 cm^{-1}. An alternative mechanism for this parallel vibronic transition would involve vibronic coupling between the vibrational levels of the $\tilde{B}\ ^2A'$ state with the nearby $\tilde{C}\ ^2A''$ state to which the higher-energy bands between 31 500–34 500 cm^{-1} are assigned below.

2. Higher-energy bands, $\tilde{C}\ ^2A'' \leftarrow \tilde{X}\ ^2A''$

The PFY spectra in Fig. 3 reveals transitions at higher photon energies starting at 31 500 cm^{-1}. The observed transitions are in excellent agreement with earlier reported absorption spectra,[26–29] in which these bands appeared simultaneously with the rotationally resolved $\tilde{B}\ ^2A' \leftarrow \tilde{X}\ ^2A''$ band of HNCN. This led Kroto and co-workers[28] and Basco and Yee[27] to associate these bands with another excited electronic state of HNCN. However, based upon isotopic substitution data and partial rotational analysis of the 31 500 cm^{-1} band, Mathews *et al.*[29] assigned the carrier of these bands near 30 500, 31 500, and 32 500 cm^{-1} to the HCNN species, an assignment we believe is incorrect. We confidently assign this transition and the higher-energy transitions to the HNCN radical based upon two observations. First, a photoelectron spectrum taken in a separate apparatus in our laboratory using the same source conditions shows that only the HNCN isomer is produced upon photodetachment.[32] Second, the experimental thresholds for $P(E_T)$ distributions for the bands between 31 500–34 500 cm^{-1} match the expected E_T^{max} values determined from the $P(E_T)$ distribution of the well-known $\tilde{B}\ ^2A' \leftarrow \tilde{X}\ ^2A''$ band of HNCN. These higher-energy bands must therefore also correspond to the HNCN isomer. For a comparison, based upon the heats of formation listed in Table II, the predicted E_T^{max} value the HCNN isomer at a photon energy of 4.035 eV is 2.91 ± 0.81 eV.[21]

Although the PFY spectra in Fig. 3 correspond to previously observed spectra, no assignments of the responsible electronic transition were made in the earlier work. The HNCN radical is isoelectronic with the linear NCO radical, which has electron configuration $\ldots(6\sigma)^2(1\pi)^4(7\sigma)^2(2\pi)^3$. The HNCN radical is bent, splitting the π orbitals into a' and a'' orbitals and yielding $\ldots(6a')^2(7a')^2(1a'')^2(8a')^2(9a')^2(2a'')^1$ for the molecular orbital configuration. The perpendicular $\tilde{B}\ ^2A' \leftarrow \tilde{X}\ ^2A''$ transition corresponds to promotion of an electron from a nonbonding $8a'$ to the $2a''$ lone pair on the hydrogen-bonded N atom. The next electronic absorption should correspond to the promotion of an electron from a strongly bonding π-type orbital, $1a''$ or $7a'$, to the out-of-plane lone pair orbital $2a''$, analogous to the $\tilde{B}\ ^2\Pi \leftarrow \tilde{X}\ ^2\Pi$ transition of the NCO radical.[44,45] An electronic transition of this type is expected to give rise to an extended progression of the HN–C–N symmetric stretch. Excitation of an electron from the $1a''$ or $7a'$ orbital yields a parallel *a*-type or perpendicular *c*-type transition, respectively.

The vibronic transitions near 32 500, 33 500, and 34 500 cm^{-1} clearly do not exhibit the sharp, well-separated K_a structure associated with the perpendicular *c*-type $\tilde{B}\ ^2A' \leftarrow \tilde{X}\ ^2A''$ transition and are instead dominated by an intense subband that looks like a red-degraded *R*-bandhead [see Fig. 3(b)]. The shape of this feature is consistent with a parallel electronic transition in which the *a*-axis rotational constants are similar so that the $\Delta K_a = 0$ bands are superimposed on each other. In addition, the vibrational progression frequency of ~1000 cm^{-1} is similar to the 1050 cm^{-1} symmetric stretch progression of the $\tilde{B}\ ^3\Sigma_u^- \leftarrow \tilde{X}\ ^3\Sigma_g^-$ band of the NCN radical,[20,28] and is in reasonable agreement with experimental values of 1140 cm^{-1} (Ref. 25) and 1146 cm^{-1} (Ref. 31) for the HN–C–N ground state symmetric stretch. Hence it is reasonable to assume that the observed progression is due to the upper state symmetric stretch. These observations suggest that the transition involves electronic excitation from the $1a''$ orbital to the $2a''$ orbital and it is assigned to the $\tilde{C}\ ^2A'' \leftarrow \tilde{X}\ ^2A''$ band.

The band structure associated with the 31 550 cm^{-1} band is particularly complex, as demonstrated by the previous misassignment of this band to the HNCN isomer.[29] Based upon the vibrational spacing, this transition appears to be a lower vibronic transition of the $\tilde{C}\ ^2A'' \leftarrow \tilde{X}\ ^2A''$ band. However, the regular subband spacing of ~24 cm^{-1} is dramatically different from the band structure of the higher-energy transitions and is not consistent with either parallel or perpendicular electronic transitions. A complicated subband structure that shifts upon deuteration has also been observed for a lower member of this progression at 30 450 cm^{-1},[26,29] this feature was not seen in our PFY spectrum, presumably because of its low quantum yield for dissociation. The band structure of the lower members of the $\tilde{C}\ ^2A'' \leftarrow \tilde{X}\ ^2A''$ band near 30 450 and 31 550 cm^{-1} may be due to perturbations by the nearby $\tilde{B}\ ^2A'$ state, similar to the strong perturbations

Downloaded 01 Jun 2001 to 128.32.220.22. Redistribution subject to AIP license or copyright, see http://ojps.aip.org/jcpo/jcpcr.jsp

TABLE II. Heats of formation of relevant $H_xC_yN_z$ species.

Species	$\Delta_f H_0$ (eV)	$\Delta_f H_{298}$ (eV)	Reference
C	7.3708±0.005	7.428±0.005	47
H	2.239±0.000 06	2.2594±0.000 06	47
N	4.8797±0.001	4.8989±0.001	47
CH	6.149±0.013	6.1846±0.013	48
NH	3.90±0.17	3.90±0.17	47
N_2	0	0	Ref. state
CN	4.513±0.021	4.498±0.021	49
CNN	6.16±0.03	6.15±0.03	21
NCN	4.83±0.03	4.82±0.03	20
HCN	1.34±0.03	1.336±0.03	50
HNC	1.92±0.04	1.95±0.04	51
HCNN	5.02±0.18	4.98±0.18	21
HNCN	3.35±0.03	3.31±0.03	This work
H_2CNN	3.09±0.20	3.03±0.02	21
H_2NCN	1.46±0.11	1.38±0.11	This work with Ref. 23

that have been observed for the corresponding $\tilde{B}\ ^2\Pi$ and $\tilde{A}\ ^2\Sigma^+$ states of NCO.[44–46]

B. Translational energy distributions

The $P(E_T)$ distributions reveal how available energy is distributed among the photofragments. The energy balance for dissociation of HNCN to $CH+N_2$ is described by Eq. (1).

$$h\nu + E_{\mathrm{INT}}(\mathrm{HNCN}) = D_0(\mathrm{HNCN}) + E_T + E_{\mathrm{VR}}(N_2) + E_{\mathrm{VR}}(\mathrm{CH}), \quad (1)$$

where $h\nu$ is the photon energy, E_{INT}(HNCN) is the average rotational energy of the parent radical about the *b* and *c* axes (≈60 K) plus the rotational energy associated with a particular K_a level. For the $\tilde{C}\ ^2A'' \leftarrow \tilde{X}\ ^2A''$ transitions, we excite the largest feature of the *R* bandhead and assume that the $K_a=0$ levels dominate this feature. D_0 is the dissociation energy, E_T is the measured translational energy, and $E_{\mathrm{VR}}(N_2)$ and E_{VR}(CH) are the internal vibrational and rotational energies of the N_2 and CH photofragments.

D_0(HNCN) for the N_2 loss channel can be extracted from these distributions so long as one can determine an accurate value for $E_T^{\max}$, the translational energy corresponding to photofragments with zero internal energy. As discussed in Sec. III C, this condition is satisfied, since the distributions all drop off sharply above a consistent value of $E_T^{\max}$. For HNCN, the sharpest onset occurs at $h\nu=3.609$ eV, yielding $D_0=2.80\pm0.02$ eV. From our experimental value for D_0, and from literature values for the photofragment heats of formation (see Table II), and heat capacities,[47] we calculate $\Delta_f H_0(\mathrm{HNCN})=3.35\pm0.02$ eV and $\Delta_f H_{298}(\mathrm{HNCN})=3.31\pm0.02$ eV. The latter is in reasonable agreement with $\Delta_f H_{298}(\mathrm{HNCN})=3.34\pm0.13$ eV derived by Clifford *et al.*[23] but smaller error bars are associated with our value. Similarly, from the $P(E_T)$ distribution for DNCN at 3.599 eV, $D_0=2.835\pm0.030$ eV and $\Delta_f H_0(\mathrm{DNCN})=3.33\pm0.03$ eV.

The $P(E_T)$ distributions also reveal the internal energy distributions of the nascent N_2 and CH photofragments. The resolved structure in these distributions reflects the photofragment vibrational distributions. The nearly identical structure of the $P(E_T)$ distributions for HNCN and DNCN at similar photon energies indicates that the observed structure is not associated with the C–H vibration and is instead due to vibration of the N_2 photofragment. Furthermore, the spacing between peak maxima ranges from 220–260 meV, in reasonable agreement with the N_2 vibrational frequency, 292 meV, compared to 354 meV for CH. The combs shown above the $P(E_T)$ distributions indicate the calculated onsets for vibrationally excited levels of the N_2 fragment. The N_2 vibrational distribution for each of the HNCN and DNCN $P(E_T)$ distributions are estimated by fitting the vibrational features of the $P(E_T)$ distributions with nearly Gaussian functions with a slightly asymmetric tail to lower translational energies. The resulting vibrational distributions and average vibrational energy, $\langle E_{\mathrm{vib}}\rangle$ are listed in Table III. Table III and Figs. 5 and 6 show that the N_2 vibrational excitation increases as a function of the overall photon energy. Increasing the photon energy from the $\tilde{B}$ state origin at 3.603 eV to the $\tilde{C}$ state at 3.911 eV shifts the $\nu=0{:}\nu=1$ vibrational population ratio from 6:1 to nearly 1:1, where ν is the vibrational state of the N_2 photofragment. At even higher photon energies, the $\nu=1$ state of N_2 dominates the vibrational distribution and the population in the $\nu=2$ and 3 states increases as well.

TABLE III. N_2 photofragment vibrational distributions and average vibrational energy for the HNCN and DNCN $P(E_T)$ distributions.

Parent molecule	Photon energy (eV)	$E_T^{\max}$ (eV)	($\nu=0$)	($\nu=1$)	($\nu=2$)	($\nu=3$)	$\langle E_{\mathrm{vib}}\rangle$ (eV)
HNCN	3.6027	0.795	85	15	···	···	0.043
	3.911	1.115	43	39	18		0.216
	4.035	1.235	31	41	25	3	0.288
	4.157	1.36	18	39	30	13	0.396
DNCN	3.599	0.764	83	17	···	···	0.049
	3.909	1.074	44	41	15	···	0.203
	4.035	1.200	33	42	24	2	0.276
Franck–Condon mapping of TS2			17.5	33.8	31.0	17.7	0.427

The peak widths and shape of the vibrational features of the $P(E_T)$ distributions are determined by the experimental energy resolution (≈20 meV) and the rotational distribution of the N_2 and CH photofragments. For each N_2 vibrational state, the most probable value for total fragment rotational energy, E_{rot}, is given by

$$E_{\mathrm{rot}} = E_T^{\max}(\nu) - E_{\mathrm{peak}}(\nu). \quad (2)$$

Here $E_{\mathrm{peak}}(\nu)$ is the translational energy of the peak maximum of a particular N_2 vibrational state and $E_T^{\max}(\nu)$ represents the maximum translational energy for that state, corresponding to photofragments with zero rotational excitation and given by

$$E_T^{\max}(\nu) = h\nu - D_0 - E_{N_2}^{\mathrm{vib}}(\nu), \quad (3)$$

where $h\nu$ is the photon energy, D_0 is the dissociation energy, and $E_{N_2}^{\mathrm{vib}}(\nu)$ is the energy for the νth vibrational state of N_2.

Table IV lists values of E_{rot} for both HNCN and DNCN. The vibrational structure is increasingly broadened for higher photon energies, making a precise determination of the peak positions less certain as reflected by the reported error bars.

Downloaded 01 Jun 2001 to 128.32.220.22. Redistribution subject to AIP license or copyright, see http://ojps.aip.org/jcpo/jcpcr.jsp

TABLE IV. Rotational energy maxima as function of N_2 vibrational quantum number.

	Photon energy (eV)	$E_{rot}(\nu=0)$ (eV)	$E_{rot}(\nu=1)$ (eV)	$E_{rot}(\nu=2)$ (eV)
HNCN	3.603	0.125±0.10	0.064±0.010	···
	3.911	0.178±0.020	0.131±0.020	0.049±0.025
	4.035	···	0.147±0.015	0.064±0.020
	4.157	0.21±0.020	0.173±0.025	0.096±0.025
DNCN	3.599	0.13±0.015	0.045±0.020	···
	3.909	0.174±0.020	0.075±0.020	0.031±0.020
	4.035	0.210±0.030	0.081±0.030	0.056±0.030

The values of E_{rot} exhibit a strong dependence on the N_2 vibrational quantum number, with higher N_2 vibrational states yielding smaller values of E_{rot}. For a given N_2 vibrational state, E_{rot} increases with photon energy. Based on the peak widths for each feature in the $P(E_T)$ distributions, higher values of E_{rot} are correlated with broader rotational distributions.

Finally, we can place limits on the rate of dissociation for the excited $\tilde{B}\ ^2A'$ state. The LIF experiments of Wu *et al.*[25] determined the fluorescence lifetime of the $\tilde{B}\ ^2A' \rightarrow \tilde{X}\ ^2A''$ transition to be 20±5 ns, so the lifetime τ_d with respect with respect to dissociation must at least be this long. An upper limit on τ_d can be obtained because delayed dissociation reduces the effective flight length between the photolysis laser and the detector (1 m). This effect transforms what would normally be an infinitely sharp peak in the $P(E_T)$ distribution to a feature with an exponential ''tail'' toward low E_T with a width on the order of $\Delta E/E_T = 2\tau_d/\tau_l$, where τ_l (~5 μs) is the flight time from the interaction region to the detector. For the HNCN $P(E_T)$ distribution at $h\nu=3.603$ eV, simulations of the peak shapes yield an upper bound of ~250 ns for τ_d, beyond which the exponential tail becomes too prominent in comparison with the experimental peaks.

V. DISCUSSION

The formation of $CH+N_2$ photofragments from the HNCN radical is an interesting and surprising result, requiring both an H-atom shift to the central carbon and bending of the NCN backbone to allow N–N bond formation, and suggesting linear or cyclic isomers of HNCN as possible intermediate structures. Such a complicated rearrangement process is expected to give rise to substantial potential energy barriers. Our goal in this section is to use the experimental product state internal energy distributions to gain insight into the barrier heights, transition state geometries, and electronic states involved in the dissociation of electronically excited HNCN to $CH+N_2$ products.

The most important trends in the experimental $P(E_T)$ distributions are that (1) they all extend toward E_T^{max} and show that most of the available energy goes into product translation, and (2) they display resolved vibrational structure characteristic of the N_2 photofragment. From (1) we infer that dissociation occurs either on a repulsive surface or through a tight transition state associated with passage over a barrier. The second observation is quite unusual and suggests a highly specific partitioning of energy among product rotational and vibrational degrees of freedom, with most of the available internal energy channeled into N_2 vibration. To our knowledge, the only other observation of a vibrationally resolved $P(E_T)$ distribution for a channel with two molecular products was in the dissociative photodetachment of O_4^-.[52] This trend is consistent with passage through a linear or cyclic HNCN transition state in which the N–N bond length differs from that of diatomic N_2, with a considerably smaller difference for the C–H bond length.

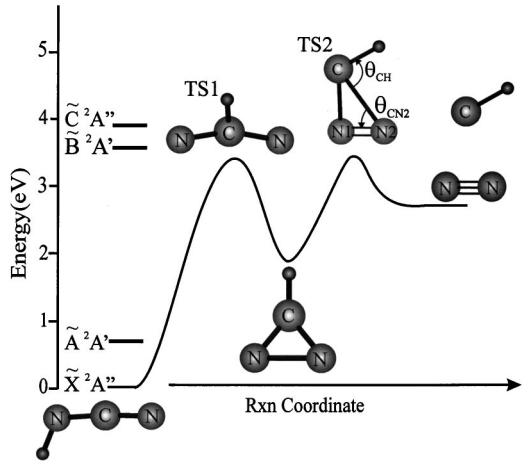

FIG. 7. Energetics of the excited states of HNCN and schematic of the overall dissociation reaction mechanism. The energetic positions of the $\tilde{X}\ ^2A''$ state is based upon this work, the term values for the $\tilde{A}\ ^2A''$, $\tilde{B}\ ^2A'$, and $\tilde{C}\ ^2A''$ states are based upon the respective spectroscopic studies, Refs. 32, 24, and 26. The structure for HNCN is based upon spectroscopic results (Ref. 21), the structure and energies for TS1 are from Ref. 13, while the TS2 and INT1 are from Ref. 12.

Ab initio calculations by Cui *et al.*,[11,12] Lin and co-workers,[13,19] and Walch[15] on the potential energy surfaces of $CH+N_2$ have identified a number of bound intermediates and transition states structures that may be relevant to the dissociation mechanism of HNCN. Of particular interest are the linear (lin-) HCNN and cyclic (c-) HCN_2 isomers calculated to lie 1.2 and 1.0 eV, respectively, below the $CH+N_2$ product channel. The linear isomer does not have an exit barrier with respect to dissociation to $CH+N_2$, so product state distributions from this intermediate should be reasonably described by statistical models such as a prior distribution,[53] which, depending on the available energy, predicts between 25%–42% of the available energy is partitioned into translation. This statistical distribution is in sharp contrast to the experimental $P(E_T)$ distributions with 61%–75% of the available energy partitioned into translation.

The reaction coordinate for dissociation of HNCN to $CH+N_2$ via c-HCN_2 is shown in Fig. 7. Two transition states are involved: TS1, the transition state for isomerization of HNCN to c-HCN_2, and TS2, the transition state for dissociation of c-HCN_2 to $CH+N_2$. The TS2 structure is a reasonable candidate for the transition state leading to the experimental $P(E_T)$ distributions. The tight three-center transition state is expected to give rise to a nonstatistical product state distribution and it is energetically accessible at

Downloaded 01 Jun 2001 to 128.32.220.22. Redistribution subject to AIP license or copyright, see http://ojps.aip.org/jcpo/jcpcr.jsp

TABLE V. Transition state bond angles and distance from the *ab initio* calculations of Cui *et al.* (Refs. 11 and 12). The bond distances for the free diatomic fragments (Ref. 54) are shown for a comparison.

	Cyclic transition state (TS2)	Diatomic fragments
R_{CH}	1.103 Å	1.1199 Å
R_{NN}	1.189 Å	1.0976 Å
R_{CN1}	1.522 Å	
R_{CN2}	1.883 Å	
θ_{CH}	81.6°	
θ_{CN2}	53.8°	
Dih H–C–N_2–N_1	−158.4°	

the photon energies used in this study. The structural parameters for TS2 calculated by Cui *et al.*[11,12] at the UCCSD(T)/6-311G(*d*,*p*) level of theory are listed in Table V, along with those of diatomic N_2 and CH; the change in N–N bond length upon dissociation is considerably larger than the change in C–H bond length, providing further motivation for considering TS2 as the relevant transition state for our experiment.

In order to be more quantitative, we compare below our experimental product state distributions with those expected from simple dissociation models involving dissociation via the TS2 transition state. The product vibrational and rotational distributions are treated separately.

A. Vibrational distributions

In this section, limiting models for the product vibrational distributions are considered assuming TS2 to be the transition state for dissociation. In the limit of rapid dissociation over a barrier the steep repulsive exit valley does not allow for coupling between vibrational and translational modes. A simple model for describing the resulting photofragment vibrational distribution is provided by a Franck–Condon (FC) mapping of the transition state equilibrium geometry onto the photofragment equilibrium bond distances.[55] As is seen in Table V, the CH bond length changes only 0.017 Å from TS2 to the free diatomic. FC mapping of the transition state produces >99% of the vibrational population in $\nu=0$. The N_2 bond distance shows a more substantial change, decreasing by ~0.09 Å from TS2, leading to a N_2 vibrational distribution that peaks at $\nu=1$ with nearly equal populations in $\nu=1$ and $\nu=2$. Table III shows that a FC mapping of the transition state, which is independent of photon energy, overestimates the extent of N_2 vibrational excitation compared to the $P(E_T)$ distribution from excitation at 3.603 eV, although it agrees well with the results at 4.157 eV.

The observed evolution of the $P(E_T)$ distributions toward higher N_2 vibration with increasing photon energy suggests that higher vibrational levels of the transition state become populated as $h\nu$ increases. An alternative description of the product vibrational distribution that accounts for this effect is the statistically adiabatic channel model (SACM).[56–58] In this model it is assumed that the vibrational levels of the transition state are statistically populated and that the vibrational quantum numbers are preserved through dissociation to product degrees of freedom. The CH and N_2 product vibrational populations are then a reflection of the populations of the CH and N_2 stretching modes at the transition state. Using the vibrational frequencies of Cui *et al.*,[11,12] and assuming that the vibrational modes are harmonic, the relative population of the vibrational levels of the transition state were calculated as a function of energy above the barrier using the Beyer–Swinehart algorithm.[58] These calculations indicate that a statistical distribution of transition state vibrational states and a barrier height of 0.5 eV above the dissociation asymptote reproduce the N_2 vibrational distribution of at 3.603 eV; this barrier height is reasonable based on the energetics in Fig. 7. However, using this same barrier height, the degree of N_2 vibrational excitation is underestimated at higher photon energies, suggesting that the vibrational populations of the transition state modes are not statistically distributed.

Overall, the experimental N_2 vibrational distributions fall between the FC and SACM model limits. The fact that neither model works over the entire range of photon energies is not entirely surprising. On the other hand, the SACM and FC models reasonably reproduce the N_2 vibrational distributions at the lowest and highest photon energies, respectively, and this limited agreement provides more quantitative support for assuming TS2 to be the transition state through which dissociation occurs.

B. Rotational distributions—modified impulsive model

The results in Table IV show that at each photon energy, E_{rot} decreases with increasing N_2 vibration. This trend suggests that the rotational distributions should be analyzed using the modified impulsive model,[59–61] which assumes that dissociation is mediated by an instantaneous repulsive force between the departing atoms and that the vibrations of the recoiling fragments are infinitely stiff. The impulse does not generate fragment vibrational excitation. The fragment vibrational distribution is formed prior to the impulse, and hence this vibrational energy, E_{vib}, is not available to translation or rotation. The impulsive fragment rotational energy, E_{rot}^{imp}, described by Eq. (4), is dependent upon the parent molecular geometry and the energy available for translation,

$$E_{rot}^{imp}=\alpha\cdot(E'_{avail})+\beta_{h\nu}, \tag{4}$$

where α describes the geometric factors as described by Buttenhoff *et al.*,[62] E'_{avail} is equal to the total energy available to the products minus the fragment vibrational energy, and $\beta_{h\nu}$ is ideally equal to zero.

The first step in assessing the suitability of this model is to determine how well the experimental data in Table IV are described by Eq. (4). The parameter α was found at each photon energy and the results are shown in Fig. 8 for HNCN and DNCN. This plot shows that the entire dataset for each species has approximately the same value of α, with slightly higher values, in general, for DNCN than HNCN. However, plots of E_{rot} vs E_{avail} have small, nonzero *y*-intercept values $\beta_{h\nu}$ that vary between −0.04 to −0.13 eV for HNCN and −0.10 to −0.14 eV for DNCN, in contrast to the predictions

Downloaded 01 Jun 2001 to 128.32.220.22. Redistribution subject to AIP license or copyright, see http://ojps.aip.org/jcpo/jcpcr.jsp

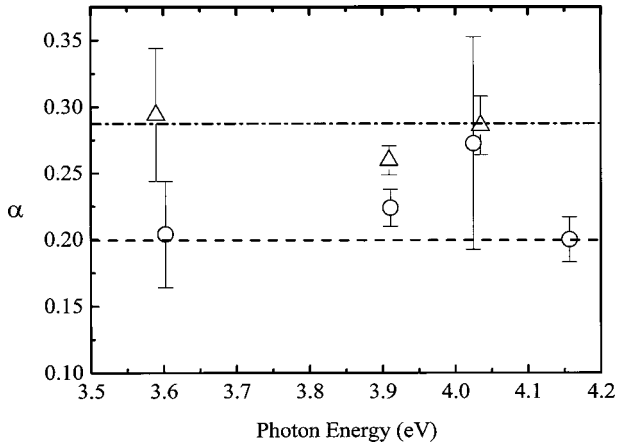

FIG. 8. Experimental values of α for the dependence of E_{rot} with E_{avail} for HNCN (○) and DNCN (△) at various photon energies (see the text). Calculated values from the modified impulsive model described in the text are shown with dashed horizontal lines. The error bars are significantly larger for data points at 3.6 and 4.0 eV since only two data points were used to determine the slope.

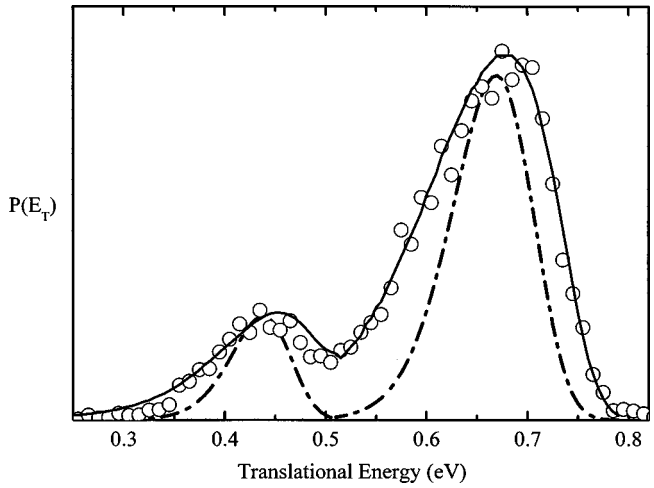

FIG. 10. A comparison of the experimental $P(E_T)$ distribution for excitation at 3.6027 eV (○) with the impulsive model calculation. The dashed–dot line is the result of the impulsive model including the zero-point vibrational motion of the transition state. The solid line includes the zero-point motion and an estimated parent rotational distribution of 100 K.

of the model. Nonetheless the relatively small variations in slope (i.e., α) suggest that the model be pursued further.

The next step is to compare the experimental values of α to predictions from the modified impulsive model, again assuming TS2 as the transition state for dissociation. For simple bond cleavage, the impulsive force is naturally applied along the breaking bond, but for three-center-type dissociations, such as c-$HCN_2 \rightarrow CH + N_2$, the impulse need not occur along an individual bond.[62] The normal modes of TS2 are shown in Fig. 9.[63] An approximate direction of the impulse can be obtained from the motion along the reaction coordinate, the ν_6 eigenvector, which is primarily associated with stretching of the long C–N bond (C–N_2). As pointed out by Buttenhoff *et al.*,[62] the impulsive force occurs in the exit valley past the transition state geometry since at the transition state itself, there is no force on the photofragments. Here, we have made the further approximation that the geometry at which the impulse is applied is that of the transition state. The impulsive force primarily excites the N_2 photofragment, e.g., a value of $E'_{\mathrm{avail}} = 0.6$ eV gives rise to rotational quantum numbers of 19 and 3 for j_{N_2} and j_{CH}, respectively. Values of α from the model calculation for HNCN and DNCN are shown as horizontal lines in Fig. 8. The larger value for the DNCN system is due to the larger impact parameter associated with the CD fragment. There is reasonable agreement with the experimental values for both species, supporting the validity of the model and the assumption of TS2 as the transition state.

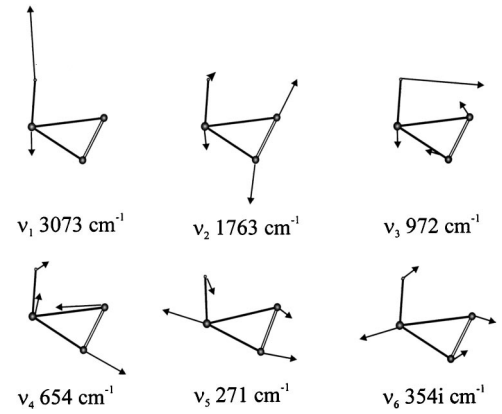

FIG. 9. Eigenvectors and eigenvalues of the normal modes for TS2 from the *ab initio* calculations of Cui *et al.* (Ref. 58). Only the motion in the C–N_1–N_2 plane is shown here; ν_5 and ν_6 possess ''out-of-plane'' H-atom motion.

The modified impulsive model provides only a single rotational energy, not a rotational distribution. Such a distribution can be obtained by including the effect of parent vibrational and rotational motion.[60] We first consider the contribution from zero-point vibrational motion. Using the eigenvectors and frequencies for the transition state normal modes[63] (Fig. 9), and following the work of Buttenhoff *et al.*,[62] we have determined the contribution of the zero-point motion of each transition state vibration toward the fragment rotational distributions. Vibrational motion in the CNN plane will have the largest effect upon the rotational distribution since the momentum will add or subtract from the impulsive momentum. Asymmetric stretching of the C–N bonds, ν_4, leads to the largest spread in the N_2 rotational distribution with a FWHM of four rotational quanta while the in-plane H-atom bending mode, ν_3, leads to a FWHM of 2 quanta for the CH fragment. Converting the rotational distribution into an energy distribution and then convoluting with our experimental energy resolution yields the dashed line in Fig. 10 for the $P(E_T)$ distribution at $h\nu = 3.603$ eV. It appears that vibrational motion does not completely account for the total width of the experimental translational energy distribution. However, following Levene and Valentini,[10] parent rotational excitation is also expected to contribute to the fragment rotational distribution resulting in further broadening. A temperature of 100 K for the rotational distribution of the transition state provides a reasonable fit to the experimental data, shown with a solid line in Fig. 10.

Downloaded 01 Jun 2001 to 128.32.220.22. Redistribution subject to AIP license or copyright, see http://ojps.aip.org/jcpo/jcpcr.jsp

The same procedure could not account for the width of the features in the $P(E_T)$ distributions at higher photon energies. This discrepancy may reflect the contribution of vibrationally excited levels of the transition state, since the larger momentum associated with higher vibrational levels should lead to a broader fragment rotational distribution. For example, the $\nu_4=1$ transition state level results in a rotational distribution with a FWHM of seven rotational quanta for the N_2 fragment. This corresponds to a width of 170 meV for the N_2 ($\nu=0$) feature of the $P(E_T)$ distribution at 3.911 eV, accounting for most of the observed width of 210 meV.

C. Dissociation mechanism

The preceding discussion strongly implies that the $CH+N_2$ products are formed by passage through the cyclic TS2 transition state. This raises the question of how electronically excited HNCN radicals access this transition state. Several observations are relevant here. The PFY spectra for excitation to the $\tilde{B}\ ^2A'$ and $\tilde{C}\ ^2A''$ states are structured, indicating predissociation rather than direct dissociation on repulsive surfaces. The $\tilde{B}$ state, in particular, is quite long lived, with a lifetime between 20 and 250 ns (Sec. IV B). The $\tilde{B}$ and $\tilde{C}$ excited states both dissociate to ground state $CH+N_2$ products. Furthermore, the extent of N_2 vibrational excitation and width of the rotational distributions appear to increase smoothly with excitation energy and do not display any obvious dependence on either the electronic or vibrational character of the optically prepared excited state.

This set of observations suggests that electronically excited HNCN undergoes internal conversion (IC), forming highly vibrationally excited HNCN in its ground $\tilde{X}\ ^2A''$ state. Once this occurs, dissociation to $CH+N_2$ can proceed along the reaction coordinate shown in Fig. 7, in which isomerization via TS1 to c-HCN_2 is followed by dissociation via TS2 to $CH+N_2$ products:

$$\mathrm{HNCN}(\tilde{B}\ \text{or}\ \tilde{C}) \xrightarrow{\mathrm{IC}} \mathrm{HNCN}(\tilde{X}) \xrightarrow{\text{isomerization}} c\text{-HNCN} \xrightarrow{\text{dissociation}} \mathrm{CH}+\mathrm{N_2}.$$

This mechanism means that our $P(E_T)$ distributions are largely a result of ground state dynamics and are therefore relevant to the combustion chemistry of the $CH+N_2$ reaction. The barrier heights for TS1 and TS2 calculated by Cui *et al.*[11,12] and Moskaleva *et al.*[19] must be approximately correct, because if they were much higher the $\tilde{B}$ state would not be able to dissociate to $CH+N_2$ products (see Fig. 7). As a consequence, our results imply that at high temperature, the $CH+N_2$ reaction can access the HNCN intermediate. We do not observe the spin-forbidden $N(^4S)+HCN$ channel, indicating that intersystem crossing subsequent to IC does not occur to any significant extent. Our results therefore indirectly support the recent proposal by Moskaleva and Lin[13–19] that the $CH+N_2$ reaction does not yield $N(^4S)+HCN$, but instead results in higher-energy, spin-allowed $H(^2S)+NCN(\tilde{X}\ ^3\Sigma_g^-)$ products through dissociation of the HNCN radical. As discussed in the Introduction, this proposal implies that in combustion, prompt NO is not formed by oxidation of N atoms produced in the $CH+N_2$ reaction but rather by subsequent chemistry of the NCN radical. It would clearly be of great interest to perform experiments on the $CH+N_2$ reaction under single-collision conditions to directly determine the identity of the products of the biomolecular reaction.

VI. CONCLUSIONS

The photodissociation dynamics and spectroscopy of the HNCN radical have been investigated. Photofragment yield spectra show that the $\tilde{B}\ ^2A'$ excited state predissociates. In addition, predissociation is seen from the previously observed absorption bands 31 500–34 500 cm^{-1}. These bands are conclusively attributed to HNCN and are assigned as the $\tilde{C}\ ^2A''\leftarrow\tilde{X}\ ^2A''$ band. At all photon energies, $CH+N_2$ is found to be the primary dissociation channel. The product state distributions are vibrationally resolved, showing vibrational progressions in the N_2 fragment. The distributions are highly nonstatistical and show an inverse relationship between rotational and vibrational excitation.

The product vibrational and rotational distributions can be reasonably well fit by applying simple models to the cyclic HCN_2 transition state geometry calculated by Cui and Morokuma,[11] suggesting that the dissociation pathway to $CH+N_2$ involves a c-HCN_2 intermediate that dissociates via a tight-three-center transition state. Based upon the variation of the product state distributions with photon energy, a dissociation mechanism is proposed in which the excited states undergo internal conversion to the ground state, followed by isomerization to c-HCN_2, which then dissociates to $CH+N_2$. Our results are generally consistent with *ab initio* barrier heights for the $CH+N_2$ reaction and imply that the HNCN radical is an important intermediate in the formation of prompt NO in a combustion environment.

ACKNOWLEDGMENTS

This research is supported by the Director, Office of Energy and Research, Office of Basic Energy Sciences, Chemical Sciences Division, of the U.S. Department of Energy under Contract No. DE-AC03-76F00098. R.T.B. would like to thank Professor C. W. Mathews for stimulating discussions and for generously providing absorption data prior to publication, Dr. Qiang Cui and Professor Keiji Morokuma for providing the eigenvectors of the cyclic transition state normal modes, and L. V. Moskoleva and Professor Lin for providing a copy of their manuscript prior to publication.

[1] J. A. Miller and C. T. Bowman, Prog. Energy Combust. Sci. **15**, 287 (1989).
[2] J. A. Miller and S. P. Walch, Int. J. Chem. Kinet. **29**, 253 (1997).
[3] M. R. Berman and M. C. Lin, J. Phys. Chem. **87**, 3933 (1983).
[4] L. J. Medhurst, N. L. Garland, and H. H. Nelson, J. Phys. Chem. **97**, 12 275 (1993).
[5] A. J. Dean, R. K. Hanson, and C. T. Bowman, in *Proceedings of the 23rd Symposium (International) on Combustion* (The Combustion Institute, Pittsburgh, PA, 1990), p. 259.
[6] C. P. Fenimore, in *Proceedings of the 13th Symposium (International) on Combustion* (The Combustion Institute, Pittsburgh, PA, 1971), p. 373.
[7] J. A. Miller, M. C. Branch, W. J. McLean, D. W. Chandler, M. D. Smooke, and R. J. Kee, in *Proceedings of the 20th Symposium (Interna-*

Downloaded 01 Jun 2001 to 128.32.220.22. Redistribution subject to AIP license or copyright, see http://ojps.aip.org/jcpo/jcpcr.jsp

tional) on Combustion (The Combustion Institute, Pittsburgh, PA, 1984), p. 373.
[8] D. Lindackers, M. Burmeister, and P. Roth, *23rd International Symposium on Combustion, 1990*, Vol. 23, p. 251 (1990).
[9] M. R. Manaa and D. R. Yarkony, J. Chem. Phys. **95**, 1808 (1991).
[10] M. R. Manaa and D. R. Yarkony, Chem. Phys. Lett. **188**, 352 (1992).
[11] Q. Cui and K. Morokuma, Theor. Chem. Acc. **102**, 127 (1999).
[12] Q. Cui, K. Morokuma, J. M. Bowman, and S. Klippenstein, J. Chem. Phys. **110**, 9469 (1999).
[13] L. V. Moskaleva and M. C. Lin, ''Colloquium on NO_x, SO_x and pollutant emission kinetics,'' 2000.
[14] J. M. L. Martin and P. R. Taylor, Chem. Phys. Lett. **209**, 143 (1993).
[15] S. P. Walch, Chem. Phys. Lett. **208**, 214 (1993).
[16] T. Seideman and S. P. Walch, J. Chem. Phys. **101**, 3656 (1994).
[17] S. P. Walch, J. Chem. Phys. **103**, 4930 (1995).
[18] T. Seideman, J. Chem. Phys. **101**, 3662 (1994).
[19] L. V. Moskaleva, W. S. Xia, and M. C. Lin, Chem. Phys. Lett. **331**, 269 (2000).
[20] R. T. Bise, H. Choi, and D. M. Neumark, J. Chem. Phys. **111**, 4923 (1999).
[21] R. T. Bise, A. A. Hoops, and D. M. Neumark, J. Chem. Phys. **113**, 1 (2000).
[22] R. T. Bise, A. A. Hoops, H. Choi, and D. M. Neumark, in *Imaging in Chemical Dynamics*, edited by A. G. Suits and R. E. Continetti (American Chemical Society, Washington, DC, 2000), p. 296.
[23] E. P. Clifford, P. G. Wenthold, W. C. Lineberger, G. A. Petersson, and G. B. Ellison, J. Phys. Chem. A **101**, 4338 (1997).
[24] G. Herzberg and P. A. Warsop, Can. J. Phys. **41**, 286 (1963).
[25] W. Wu, G. Hall, and T. J. Sears, J. Chem. Soc., Faraday Trans. **89**, 615 (1993).
[26] G. Herzberg and D. N. Travis, Can. J. Phys. **42**, 1658 (1964).
[27] N. Basco and K. K. Yee, Chem. Commun. (Cambridge) **3**, 150 (1968).
[28] H. W. Kroto, T. F. Morgan, and H. H. Sheena, Trans. Faraday Soc. **66**, 2237 (1970).
[29] C. W. Mathews, B. S. Pappas, and D. A. Ramsay, in *NRC Spectroscopy Conference in Memory of Gerhard Herzberg*, Ottawa, Canada, 1999.
[30] S. Yamamoto and S. Saito, J. Chem. Phys. **101**, 10 350 (1994).
[31] G. Maier, J. Eckwert, A. Bothur, H. P. Reisenauer, and C. Schmidt, Liebigs Ann. **7**, 1041 (1996).
[32] Z. Liu, R. T. Bise, and D. M. Neumark (unpublished).
[33] F.-M. Tao, W. Klemperer, M. C. McCarthy, C. A. Gottlieb, and P. Thaddeus, J. Chem. Phys. **100**, 3691 (1994).
[34] D. J. Leahy, D. L. Osborn, D. R. Cyr, and D. M. Neumark, J. Chem. Phys. **103**, 2495 (1995).
[35] R. E. Continetti, D. R. Cyr, R. B. Metz, and D. M. Neumark, Chem. Phys. Lett. **182**, 406 (1991).
[36] D. L. Osborn, H. Choi, D. H. Mordaunt, R. T. Bise, D. M. Neumark, and C. M. Rohlfing, J. Chem. Phys. **106**, 3049 (1997).
[37] D. L. Osborn, D. J. Leahy, D. R. Cyr, and D. M. Neumark, J. Chem. Phys. **104**, 5026 (1996).
[38] T. R. Taylor, R. T. Bise, K. R. Asmis, and D. M. Neumark, Chem. Phys. Lett. **301**, 413 (1999).
[39] J. M. B. Bakker, J. Phys. E **6**, 785 (1973).
[40] J. M. B. Bakker, J. Phys. E **7**, 364 (1974).
[41] D. P. de Bruijn and J. Los, Rev. Sci. Instrum. **53**, 1020 (1982).
[42] G. Herzberg, *Molecular Spectra and Molecular Structure III. Electronic Spectra and Electronic Structure of Polyatomic Molecules* (Van Nostrand Reinhold, New York, 1966).
[43] P. S. H. Bolman and J. M. Brown, Chem. Phys. Lett. **21**, 213 (1973).
[44] R. N. Dixon, Can. J. Phys. **38**, 10 (1960).
[45] R. N. Dixon, M. J. Trenouth, and C. M. Western, Mol. Phys. **60**, 779 (1987).
[46] S. A. Wright and P. J. Dagdigian, J. Chem. Phys. **104**, 8279 (1996).
[47] M. W. Chase, Jr., J. Chem. Phys. **9**, 1 (1998).
[48] M. Danielsson, P. Erman, A. Hishikawa, M. Larsson, R.-K. E. Sumame, and G. Sundström, J. Chem. Phys. **98**, 9405 (1993).
[49] Y. Huang, S. A. Barts, and J. P. Halpern, J. Phys. Chem. **96**, 425 (1992).
[50] E. P. Clifford, P. G. Wenthold, W. C. Lineberger, G. A. Petersson, K. M. Broadus, S. R. Kass, S. Kato, C. H. DePuy, V. M. Bierbaum, and G. B. Ellison, J. Phys. Chem. A **102**, 7100 (1998).
[51] A. Hansel, C. Scheiring, M. Glantschniq, and W. Lindinger, J. Chem. Phys. **109**, 1748 (1998).
[52] C. R. Sherwood, M. C. Garner, K. A. Hanold, K. M. Strong, and R. E. Continetti, J. Chem. Phys. **102**, 6949 (1995).
[53] R. D. Levine, in *Theory of Chemical Reaction Dynamics*, edited by M. Baer (CRC, Boca Raton, FL, 1985), Vol. IV, p. 1.
[54] K. P. Huber and G. Herzberg, *Constants of Diatomic Molecules* (Van Nostrand Reinhold, New York, 1979).
[55] R. Schinke, *Photodissociation Dynamics* (Cambridge University Press, Cambridge, 1993).
[56] M. Quack and J. Troe, Ber. Bunsenges. Phys. Chem. **58**, 240 (1974).
[57] M. Quack and J. Troe, Ber. Bunsenges. Phys. Chem. **79**, 469 (1975).
[58] T. Baer and W. L. Hase, *Unimolecular Reaction Dynamics* (Oxford University Press, New York, 1996).
[59] G. E. Busch and K. R. Wilson, J. Chem. Phys. **56**, 3626 (1972).
[60] H. B. Levene and J. J. Valentini, J. Chem. Phys. **87**, 2594 (1987).
[61] A. F. Tuck, J. Chem. Soc., Faraday Trans. **73**, 689 (1977).
[62] T. J. Buttenhoff, K. L. Carleton, and C. B. Moore, J. Chem. Phys. **92**, 378 (1990).
[63] Q. Cui and K. Morokuma (private communication).

Downloaded 01 Jun 2001 to 128.32.220.22. Redistribution subject to AIP license or copyright, see http://ojps.aip.org/jcpo/jcpcr.jsp